catalysts

MDPI

Article

Engineering the Integration of Titanium and Nickel into Zinc Oxide Nanocomposites through Nanolayered Structures and Nanohybrids to Design Effective Photocatalysts for Purifying Water from Industrial Pollutants

Osama Saber [1,2,*], Aya Osama [1], Nagih M. Shaalan [1,3] and Mostafa Osama [1]

[1] Department of Physics, College of Science, King Faisal University, P.O. Box 400, Al-Ahsa 31982, Saudi Arabia; ayamohamed19984@yahoo.com (A.O.); nmohammed@kfu.edu.sa (N.M.S.); mostafa.osama8664@gmail.com (M.O.)
[2] Egyptian Petroleum Research Institute, Nasr City, P.O. Box 11727, Cairo 11765, Egypt
[3] Physics Department, Faculty of Science, Assiut University, Assiut 71516, Egypt
* Correspondence: osmohamed@kfu.edu.sa; Tel.: +966-13-589-9440

Abstract: Water pollution is one of the main challenges currently facing scientists around the world because of the rapid growth in industrial activities. On this basis, 2D nanolayered and nanohybrid structures, which are based on a ternary system of nickel–titanium–zinc, are considered favorable sources for designing effective nanocomposites for the photocatalytic degradation of industrial pollutants in a short period of time. These nanocomposites were designed by modifying two-dimensional nanolayers to produce a three-dimensional porous structure of multi-doped Ni/Ti-ZnO nanocomposites. Additionally, another additive was produced by constructing nanohybrids of nickel–titanium–zinc combined with a series of hydrocarbons (*n*-capric acid, myristic acid, stearic acid, suberic acid, and sebacic acid). Energy-dispersive X-ray spectrometry, X-ray diffraction, scanning electron microscopy, infrared spectroscopy, and thermal analyses confirmed the growth of the nanolayered and nanohybrid materials in addition to the production of nanocomposites. The positive role of the dopants (nickel and titanium) in producing an effective photocatalyst was observed through a significant narrowing of the band gap of zinc oxide to 3.05–3.10 eV. Additionally, the high photocatalytic activity of this nanocomposite enabled the complete removal of colored dye from water after 25 min of UV radiation. In conclusion, this study proposes an unconventional approach for designing new optical nanocomposites for purifying water. Additionally, it suggests a novel supporting method for designing new kinds of nanohybrids based on multi-metals and organic acids.

Keywords: removal of pollutants; photodegradation of dyes; inorganic/organic nanohybrids; ternary system of nanolayers; Ni/Ti/Zn nanocomposites; low band gap energy

Citation: Saber, O.; Osama, A.; Shaalan, N.M.; Osama, M. Engineering the Integration of Titanium and Nickel into Zinc Oxide Nanocomposites through Nanolayered Structures and Nanohybrids to Design Effective Photocatalysts for Purifying Water from Industrial Pollutants. *Catalysts* **2024**, *14*, 340. https://doi.org/10.3390/catal14060340

Academic Editor: Dinesh Kumar

Received: 25 April 2024
Revised: 22 May 2024
Accepted: 22 May 2024
Published: 24 May 2024

1. Introduction

Around the world, dangers have emerged in environmental settings because of the rapid expansion of industrial and human activities. These harms are focused on water resources because various industrial pollutants are released into lakes, rivers, and oceans. These environmental- and water-related problems are especially dangerous when they relate to organic textile dyes, which are not easily biodegraded and constitute hazardous pollutants. The conventional methods used to solve these problems are not appropriate for these different kinds of pollutants because they can produce more dangerous substances as secondary pollutants. Consequently, procedures that convert organic pollutants to carbon dioxide and water using light are a promising means of solving these environment- and water-related problems. Photocatalytic processes are a kind of benign light-based technique whereby light is used as an energy source to excite photoactive materials and produce strong oxidizing agents that convert the organic pollutants to CO_2 and water. Previous

studies of photocatalytic processes [1–3] concluded that the structure of the photocatalysts plays an important role in increasing their photo-related activities and the efficiency of the photocatalytic processes. Saber et al. [1,2] designed novel nanohybrids based on inorganic–magnetic–organic structures for increasing the performance of photocatalysts to remove dyes from water. In addition, Ljubas et al. [3] utilized nanostructured titanium oxide on a glass with a simulated solar radiation lamp for the complete removal of pharmaceutical compounds from water through photocatalytic processes.

Multi-metal nanostructures are considered to be effective nanomaterials for modifying the optical properties of photocatalysts. Among these nanomaterials, layered double hydroxide (LDH) is suitable for these purposes because the cationic nanolayers of LDH consist of di-, tri-, and tetravalent metals. In addition, these nanolayers contain different kinds of anionic compounds, such as cyanate, carbonate, and nitrate, which are used as pillars for building nanolayered structures. The presence of different kinds of metals and compounds inside these nanolayered structures enables the modification and control of the crystalline structures of the nanomaterials, meaning that they can be used in a wide range of applications.

The previous studies of Xu et al. [4–6] concluded that nanolayered structures based on Al/Zn and Ti/Zn LDHs are a good means of producing photoactive nanomaterials. By controlling for the edges of the valence and conduction bands, the photocatalytic activity of doped zinc oxide could be increased to remove different kinds of aromatic pollutants [7–9]. In addition, the products of Al/Zn and Ti/Zn LDHs are sufficiently sensitive for the photocatalytic degradation of pollutants because the low band gap energy (~3.1 eV) accelerates the growth of OH radicals, which are used to decompose organic pollutants [10–13]. Along similar lines, photocatalysts have been developed and modified by several researchers via intercalation and thermal processes in addition to the surface treatment of Zn-containing LDHs [14,15].

Several studies on LDHs showed their potential applications in the photocatalytic degradation of industrial pollutants such as carboxylic acids, phenolic derivatives, the azo-group of dyes, and the xanthene group of dyes [16]. Xu et al. [17] indicated that the cationic dye of methylene blue (MB) was removed from water using the photocatalytic capacity of polyoxometalate-intercalated layered double hydroxides. Also, they concluded that the intercalation of a large cluster anion into Zn-Al-Fe LDH could endow it with not only the adsorption function of a cationic dye but also the photocatalytic performance of ZnAlFe LDH materials. Mohapatra and Parida [16] reported in their review that the flexible properties of the layered structure in LDHs play an important role in the photocatalytic processes compared with bulk photocatalysts without a layered structure. They indicated that layered materials provide a more favorable environment for the diffusion and separation of photoexcited charge carriers. Shao et al. [18] synthesized Zn/Ti layered double hydroxides with different Zn/Ti ratios for the decomposition of methylene blue (MB) under visible-light irradiation. They found that all the Zn–Ti LDHs exhibited higher photocatalytic activity than commercial TiO_2 and ZnO. Xia et al. [19] studied a series of Zn/Al, Zn/Fe, Zn/Ti, and Fe/Ti LDHs for the photocatalytic degradation of Rhodamine B dye, indicating that Zn/Ti LDH showed the best activity. Moreover, Ni/Ti LDHs [20] were synthesized and compared with ZnO, ZnS, NiO, TiO, and Degussa P25 for the photocatalytic degradation of methylene blue dye. The as-prepared LDH displayed high activity because of its lower band gap. In the same trend, the application of Zn/Cr LDHs in the photocatalytic degradation of dyes (xanthene dyes) and substituted phenol (4-chloro 2-nitrophenol) indicated the positive role of chromium ions in Zn/CrLDHs [21]. Wei and co-workers [22] indicated that a group of Cu/Ni/Zn–Cr LDHs exhibited remarkable activity regarding the photocatalytic decomposition of industrial dyes (SulphoRhodamine B, Congo red, chlorinated phenol, and salicylic acid) under visible-light irradiation.

Although several studies of LDH materials [16–26] have focused on removing pollutants using photocatalytic and adsorption techniques, a search of the literature returns no results for the Ni–Ti–Zn nanolayered structures and their nanohybrids or nanocomposites,

in addition to the dual Ni/Ti doped zinc oxide, or their applications in the photocatalytic degradation of green dyes.

Therefore, this study can achieve multiple objectives relevant to the construction of the 2D nanolayered structures of a ternary system of nickel–titanium–zinc. We propose a new approach for doping zinc oxide structures using di- and tetravalent metals in an ordered arrangement. In addition, we introduce effective photocatalysts for use in water purification. Furthermore, this study provides a novel support method for constructing a wide range of hetero-structured nanohybrids based on multi-metals and organic compounds. These achievements depend on the preparation of nanolayered structures containing a tripartite system of metals: zinc, titanium, and nickel. This tripartite system is combined with different kinds of organic compounds (*n*-capric acid, myristic acid, stearic acid, suberic acid, and sebacic acid) to produce novel nanohybrids for the first time. Additionally, this tripartite system is modified using thermal processes to generate three-dimensional porous structures of multi-doped Ni/Ti-ZnO nanocomposites. The optical properties and photocatalytic activity of these materials mean that they can be used to purify water polluted by industrial dyes using UV light. In addition, the kinetic principles are analyzed to measure the rate of acceleration of the photocatalytic decomposition of the green dyes.

2. Results

2.1. Characterizations of the Ni–Ti–Zn Nanolayers and Ni–Ti–Zn–Organic Nanohybrids

The XRD diagrams of the Ni–Ti–Zn LDH nanolayered structures and their nanohybrids are displayed in Figures 1 and 2. In addition, the XRD data are summarized in Table 1.

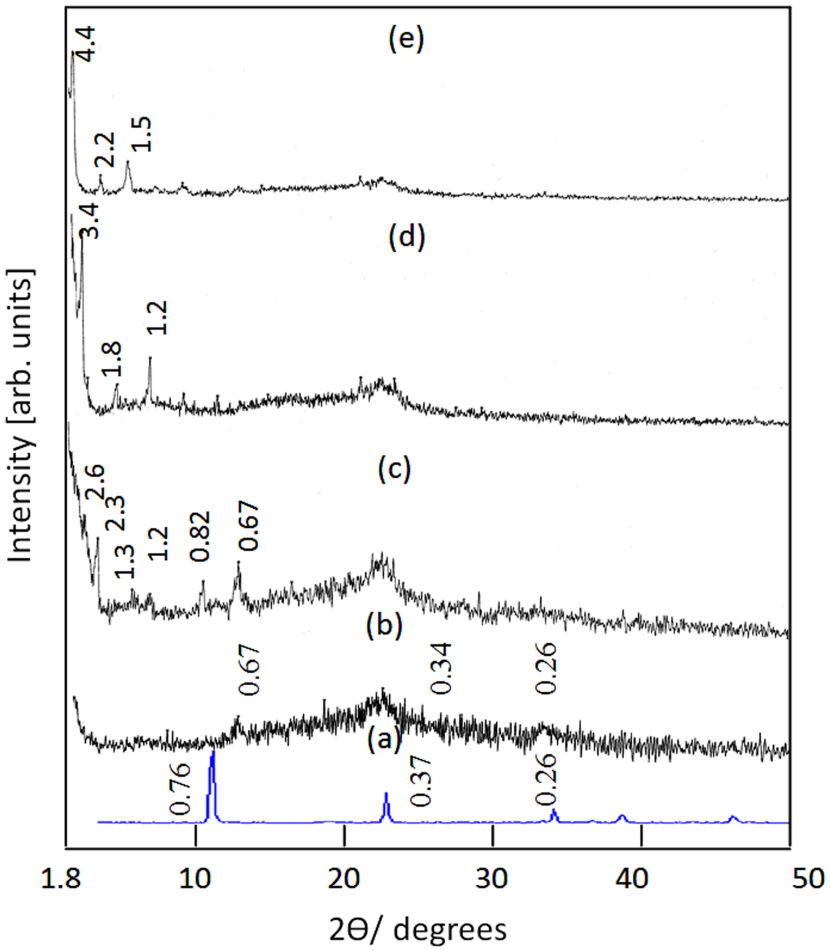

Figure 1. XRD diagrams of (**a**) Al/Zn LDHs and (**b**) Ni–Ti–Zn LDHs before intercalation reactions and after intercalation reactions with (**c**) *n*-capric acids, (**d**) myristic acids, and (**e**) stearic acids. The numbers inside the figure represent d-spacing in nm.

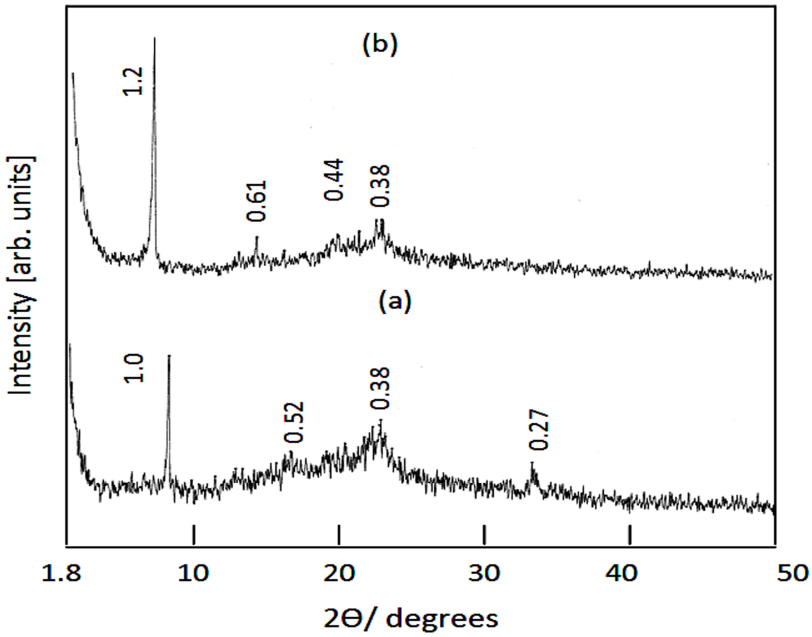

Figure 2. XRD diagrams of the Ni–Zn–Ti LDHs with the intercalation reactions of (**a**) suberic acid and (**b**) sebacic acid. The numbers inside the figure represent d-spacing in nm.

Table 1. Synthesis conditions and X-ray diffraction data of the nanolayered structures and nanohybrids.

The Nanolayered Structures	The Main Guest	Synthesis Temp. (°C)	d_{003} (nm)	Peaks in XRD (nm)	Peaks (2Θ)
Zn-Al LDH	Carbonate	80	0.76	0.76, 0.37, 0.26	11.7, 24.3, 34.3
Ni-Zn-Ti LDH	Carbonate	80	0.67	0.67, 0.34, 0.26	13.3, 26.3, 34.3
Ni-Zn-Ti-CB10	*n*-capric acid $CH_3(CH_2)_8COOH$	60	2.6	2.6, 2.3, 1.3, 1.2, 0.82, 0.67	3.4, 3.8, 6.7, 7.3 10.8, 13.3
Ni-Zn-Ti-CB14	Myristic acid $CH_3(CH_2)_{12}COOH$	60	3.4	3.4, 1.8, 1.2	2.6, 4.9, 7.3
Ni-Zn-Ti-CB18	Stearic acid $CH_3(CH_2)_{16}COOH$	60	4.4	4.4, 2.2, 1.5	2.0, 4.0, 5.9
Ni-Zn-Ti-CD6	Suberic acid $(COOHC_6H_{12}COOH)$	60	1.0	1.0, 0.52, 0.38, 0.27	8.8, 16.9, 23.6, 33.6
Ni-Zn-Ti-CD8	Sebacic acid $(COOHC_8H_{16}$ COOH)	60	1.2	1.2, 0.61, 0.44, 0.38	7.3, 14.5, 20.4, 23.4

Additionally, the XRD diagram of the Zn/Al LDH, which was prepared for comparison, is presented in Figure 1a. It showed three peaks agreeing with the layered structure of the natural hydrotalcite (JCPDS file No. 37-629) and the synthetic Zn/Al LDH (JCPDS file No. 48-1022). It exhibited sharp reflection for the basal plane (003) at d-spacing 0.76 nm. In addition, the reflections of the planes (006) and (009) were clear at 0.37 nm and 0.26 nm, respectively. Figure 1b shows three weak peaks at 2Θ = 13.3°, 25.4°, and 34.8° for the prepared Ni–Ti–Zn LDH, corresponding to the d-spacing at 0.67 nm, 0.34 nm, and 0.26 nm, respectively. The low crystallinity of Ni–Ti–Zn LDHs is due to the presence of tetravalent titanium inside the nanolayers causing strong repulsion between the cationic nanolayers because titanium creates positive charges (+2). By intercalating the long chains of organic compounds, the crystallinity of the Ni–Ti–Zn LDH increased because the long chains of the hydrocarbons expanded and widened the interlayered space among the nanolayers to avoid the repulsion between the cationic nanolayers. By conducting a comparison among the d-spacing of the three peaks of the Ni–Ti–Zn LDH, we found that the first peak is coincident with the double of the second peak and equals the third peak multiplied by three. The presence of these peaks indicates that the Ni–Ti–Zn LDH has

nanolayered structures in accordance with the reflections of the basal planes, [003], [006], and [009].

The comparison between the Al/Zn/carbonate LDHs and the prepared Ni–Ti–Zn LDHs indicated that the main d-space of Ni–Ti–Zn LDHs (0.67 nm) is smaller than that of Zn/Al LDHs (0.76 nm). According to the results of previous studies [27,28], the d-space of the LDHs decreased from 0.76 nm to 0.67 nm after drying at 150 °C because of the removal of the interlayered water. In the current study, the narrowing of the d-spacing of the Ni–Ti–Zn LDH can be attributed to the strong attraction forces between the cationic layer and the interlayered anions because the insertion of tetravalent titanium creates stronger positive charges inside the nanolayers of the Ni–Ti–Zn LDH than in the Zn -Al LDH. These positive charges (+2) are attracted by the negative charges of the carbonate anions (−2), leading to the narrowing of the interlayered spacing of the Ni–Ti–Zn LDH. By comparing with the literature data for Zn–Ti LDH [29], Zn–Al–Ti LDH [30], and Zn–Al–Sn LDH [31], the reduction in the interlayered spacing of the Ni–Ti–Zn LDH (0.67 nm) was completely similar to that observed in the results of Tagaya and Saber [29] for the interlayered d-spacing of Zn–Ti LDH. Similar results were published for Zn–Al–Sn LDH [30] because the presence of the tetravalent element (Sn) inside the LDH structure caused similar reduction in the d-spacing of Zn–Al–Sn LDH to 0.67 nm. In addition, other reports [31,32] concluded that Zn–Al–Ti LDH and Zn–Si LDH have smaller interlayered d-spacing than the conventional LDHs. They indicated that Zn–Al–Ti LDH and Zn–Si LDH have two interlayered d-spacings of 0.67 nm and 0.76 nm.

In order to avoid the narrowing of the interlayered spacing of the Ni–Zn–Ti LDH, organic–inorganic nanohybrids were used to widen and expand the interlayered space of the LDHs to clarify the layered structures of Ni–Zn–Ti LDHs. Through host–guest interactions, two kinds of nanohybrids were prepared; the first was based on monocarboxylic organic acids (*n*-capric, myristic, and stearic) and the second used dicarboxylic organic acids (suberic and sebacic). The combination of *n*-capric acid with the Ni–Zn–Ti LDH enabled the development of intercalating chains of ten carbons between the nanolayers, producing the nanolayered structures of Ni–Zn–Ti–CB10 nanohybrids. The crystalline structure of the nanolayered structures of the Ni–Zn–Ti–CB10 nanohybrids was obvious, as shown in the XRD pattern in Figure 1c. Additionally, there was a clear expansion of the interlayered space from 0.67 nm to 2.3–2.6 nm, confirming the nanolayered structure of Ni–Zn–Ti–CB10 nanohybrids. Further expansion was observed in the nanolayered structure when longer chains of carbons were intercalated using myristic acid inside the Ni–Zn–Ti LDH. The intercalation of the chains of fourteen carbons formed new nanohybrids of Ni–Zn–Ti–CB14, as shown in Figure 1d. The XRD pattern of Ni–Zn–Ti–CB14 shows a sharp peak at an acute angle with interlayered spacing of 3.4 nm. When the angles of the XRD were increased, two weak peaks were observed at 1.8 nm and 1.2 nm, as shown in Figure 1d. By analyzing this interlayered spacing, we found that the interlayered spacing of the first peak (3.4 nm) is nearly equal to twice the second value (2 × 1.8 nm) and is also almost three times larger than the third value (3 × 1.2 nm). This result confirms the nanolayered structure of Ni–Zn–Ti–CB14. In the case of using stearic acids, which have very long chains of carbon (18 carbons), strong expansion was observed between the nanolayers in the crystalline structure of Ni–Zn–Ti–CB14, as shown in the XRD pattern. Figure 1e shows the XRD pattern of Ni–Zn–Ti–CB18. A sharp peak was observed at the very small angle of 2.01° corresponding to the interlayered spacing of 4.4 nm. In addition, Figure 1e reveals two small peaks at 2.2 nm and 1.5 nm. The relation between the first peak and the other two peaks indicated the equal relationship between the interlayered spacing of the first, second, and third values, (4.4 nm), (2 × 2.2 nm), and (3 × 1.5 nm), which is clear evidence for the nanolayered structure of Ni–Zn–Ti–CB18. These results agree with the published data by Muramatsu et al. [33]. For intercalation with *n*-capric acid, Muramatsu et al. indicated that the XRD results of the intercalation products of Zn-Mo LDH showed a sharp peak at 2.51 nm agreeing with the intercalation products of the Ni–Ti–Zn LDH, which showed sharp peaks at 2.3–2.6 nm.

The other type of Ni–Zn–Ti–organic nanohybrid is based on the organic acids that have two carboxylic groups in addition to the chain of carbon, such as suberic acids ($COOHC_6H_{12}COOH$) and sebacic acids ($COOHC_8H_{16}$ COOH). These kinds of organic acids have a different effect on the prepared nanohybrids than that reported for the previous series because these organic acids have two functional groups at their ends. This means that they can react with two nanolayers at the same time. Therefore, the expansion between the nanolayers is limited and restricted by the two ends of the organic acid. This behavior became clear after the reaction between suberic acid (which has six carbons and two functional groups) and the nanolayers of Ni–Zn–Ti LDH. The XRD pattern of the Ni–Zn–Ti–CD6 nanohybrids showed only one sharp peak at an angle of 8.8°, as shown in Figure 2a. This peak corresponds with the interlayered spacing of 1.0 nm. This finding was confirmed by the reaction with sebacic acid, which has eight carbons and two functional groups; it reacted with the nanolayers to produce Ni–Zn–Ti–CD8 nanohybrids. Figure 2b shows the XRD pattern of the Ni–Zn–Ti–CD8 nanohybrids. A strong reflection was detected at an angle of 7.35°, producing interlayered spacing of 1.2 nm. Additionally, Figure 2b shows two weak peaks at 0.61 nm and 0.44 nm. The arrangement of the peaks ($1.2 \approx 2 \times 0.61$ nm $\approx 3 \times 0.44$ nm) confirmed the nanolayered structure of the Ni–Zn–Ti–CD8 nanohybrid. These results of the interlayered spacing of Ni–Zn–Ti–CD6 and Ni–Zn–Ti–CD8 agree with the published data of the intercalation compounds of Zn–Ti LDH and Zn–Al–Ti LDH [29–32].

In order to convert the two-dimensional nanolayered structures into three-dimensional nanocomposites, thermal reactions were carried out for Ni–Zn–Ti LDH at 500.0 °C and 900.0 °C. Figure 3a shows the XRD diagram of Ni–Zn–Ti–500. It is clear that the peaks of the layered structures disappeared. This means that the interlayered compounds evaporated and were removed via thermal reactions. In addition, Figure 3a shows new peaks of angles 31.8°, 34.6°, 35.2°, 43.1°, and 46.8° corresponding to d-spaces at 0.28 nm, 0.26 nm, 0.25 nm, 0.21 nm, and 0.19 nm, respectively. This means that the nanolayers of the Ni–Zn–Ti LDH re-crystallized at 500 °C to produce new structures based on the zincite phase of zinc oxide (JCPDS No. 5-644). In addition, another new phase was confirmed by observing the main reflection of the nickel zinc oxide structure (JCPDS No. 75-271) at $2\Theta = 43.14°$.

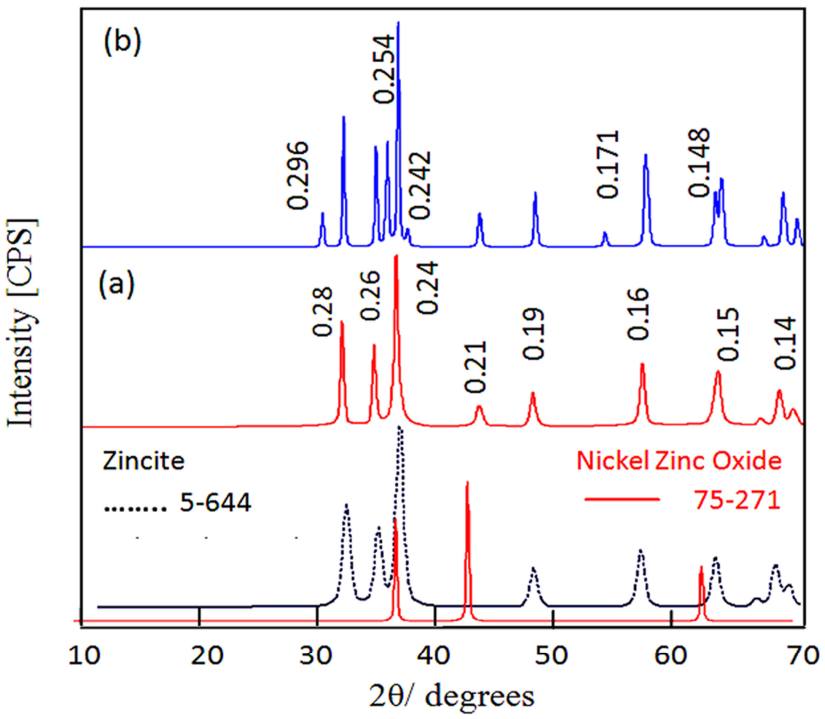

Figure 3. XRD diagrams of the Ni–Zn–Ti LDH with thermal treatment at (**a**) 500.0 °C and (**b**) 900.0 °C. The numbers inside the figure represent d-spacing in nm.

After the calcination of the prepared Ni–Zn–Ti LDH at 900.0 °C, a new series of peaks were observed, as shown in Figure 3b. Figure 3b shows clear peaks at 2Θ = 30.20°, 35.37°, 37.13°, 53.49°, and 62.50°. These peaks can be attributed to zinc titanium oxide in agreement with JCPDS No. 73-579. In addition, the original peaks of both the zinc oxide and nickel zinc oxide did not disappear, indicating that the Ni–Zn–Ti–500 and Ni–Zn–Ti–900 samples are composed of multi-oxides.

The thermal behavior of Ni–Zn–Ti LDH and its nanohybrids was studied using two techniques: differential thermogravimetric (DTG) and thermogravimetric analysis (TGA). The thermogravimetric curve of the Ni–Zn–Ti LDH, which is shown in Figure 4a, shows three weight losses. As is the case in conventionally layered double hydroxides, these weight losses are due to the evaporation of water, the decomposition of the interlayered anions, and the dehydroxylation process, respectively. These explanations for the weight losses have already been reported for Zn–Al LDH, Zn–Ti LDH, and Zn–Al–Ti LDH by many researchers [27–32]. The amount of water removed was 8.9%, and the process was completed at 240 °C. In the temperature range of 240–331 °C, the thermal decomposition led to the removal of 16.1% of the Ni-Zn-Ti LDH, corresponding to the amount of the interlayered anions. The last weight loss (5%) was achieved and completed at 795 °C. Figure 4c shows the DTG curve, which features a broad peak at 310 °C. This broad peak corresponds with the main weight loss of the Ni–Zn–Ti LDH.

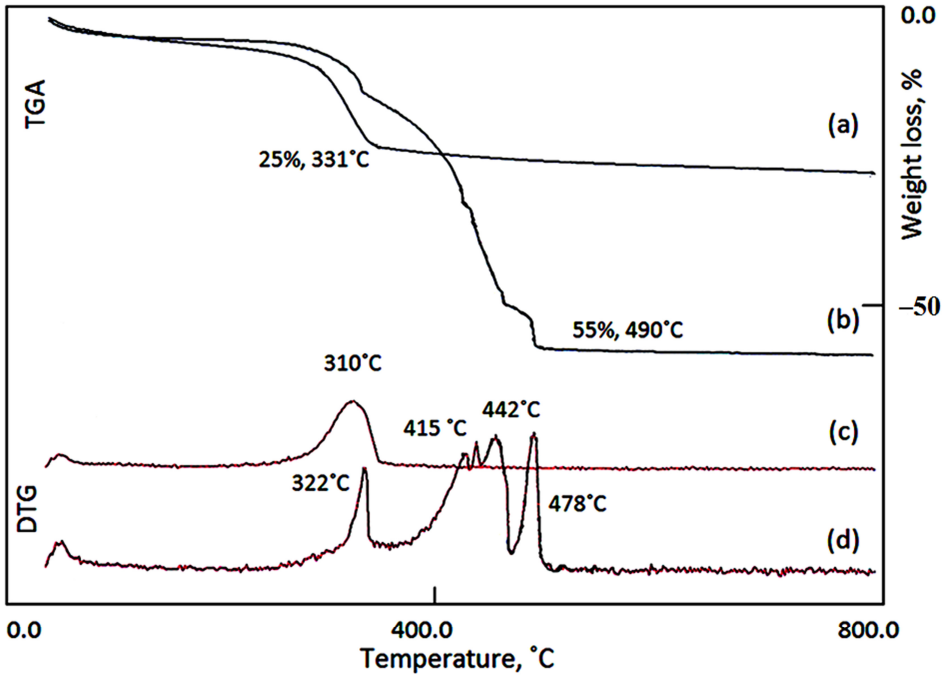

Figure 4. Thermogravimetric and differential thermogravimetric curves of the (**a**–**c**) Ni–Zn–Ti LDHs and (**b**–**d**) Ni–Zn –Ti–CD8 nanohybrids.

The thermal behavior of the Ni–Zn–Ti–CD8 nanohybrids was studied and compared with the LDHs to confirm the formation of organic–inorganic nanohybrids. Figure 4b shows the thermogravimetric curve of the Ni– Zn–Ti–CD8 nanohybrids. Based on a comparison with the parent LDHs, the number of interlayered anions in the Ni–Zn–Ti–CD8 nanohybrids increased from 16.1% to 47%, confirming the formation of nanohybrids via an anion exchange process from carbonate anions to organic anions. This large change in the number of the interlayered anions is due to the high molecular weight of organic compounds ($COOC_8H_{16}COO$). This finding was confirmed by the results of the DTG curve. Figure 4d shows the DTG curve of the Ni–Zn–Ti–CD8 nanohybrids. Four upward peaks were observed at 322 °C, 415 °C, 442 °C, and 478 °C corresponding to the decomposition of the organic compounds inside the nanolayers of Ni–Zn–Ti–CD8. These results agree with

the data published for the intercalation of the same organic compound with the Zn–Ti LDH and Zn–Al–Ti LDH [29,30].

In order to analyze these thermal processes in details and identify the kind of chemical reactions happening inside the product during heating, differential thermal analyses (DTA) were measured for the Ni–Zn–Ti LDHs and the Ni–Zn–Ti–CD8 nanohybrids. For the parent LDHs, the DTA curve of the Ni-Zn-Ti LDHs is displayed in Figure 5a. It revealed only one endothermic peak at 310 °C. This peak corresponds to the thermal degradation of carbonate anions without oxidation reaction agreeing with the results of Tagaya and Saber [32]. This means that the LDH absorbed heat to decompose carbonate anions. Meanwhile, Figure 5b shows five downward exothermic peaks at 322 °C, 415 °C, 426 °C, 455 °C, and 491 °C in the DTA diagram of the nanohybrid. These downward exothermic peaks indicate that a large amount of heat released during the decomposition process of the nanohybrid because of the oxidation reactions of the organic compounds. This explanation agrees with the results of Tagaya and Saber [29]. They reported that the decomposition temperature of the pure sebacic acid was 286 °C and, after intercalation with the Zn–Ti LDH, the temperature shifted to a higher value, confirming the formation of Zn–Ti–sebacic nanohybrids. In the current study, after the intercalation of sebacic acid with the Ni–Zn–Ti LDH, the decomposition temperature shifted to higher values, as shown in Figure 5b. This result confirmed the presence of organic compounds inside the Ni–Zn–Ti–CD8 nanohybrids. In summary, the thermal behavior of the Ni–Zn–Ti LDHs confirmed the formation of a nanolayered structure of layered double hydroxides, and the thermal properties of Ni–Zn–Ti–CD8 confirmed the formation of organic–inorganic nanohybrids.

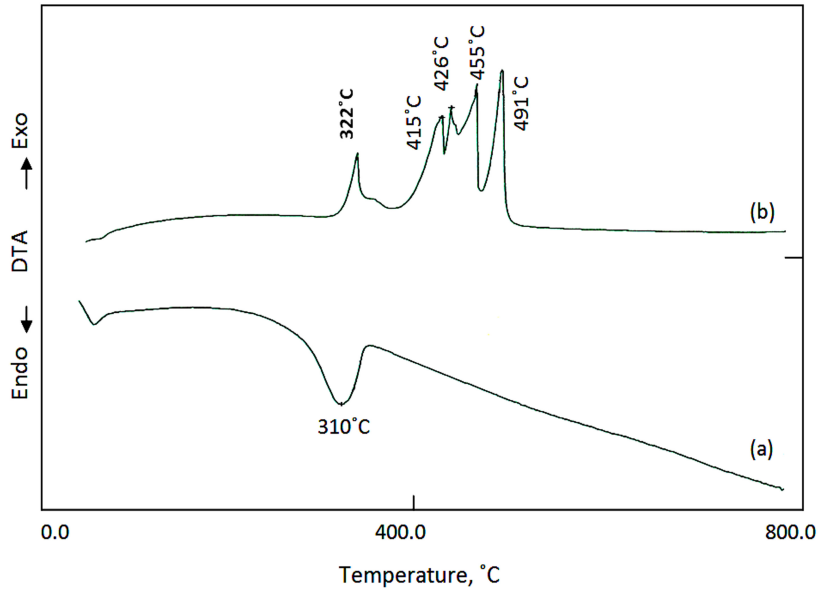

Figure 5. DTA curves of (**a**) Ni–Zn–Ti LDHs and (**b**) Ni–Zn–Ti–CD8 nanohybrids.

The structure and functional groups of the Ni–Zn–Ti LDHs were identified using the FTIR analysis, as shown in Figure 6. The hydroxyl groups of the nanolayers of LDH were identified with reference to a wide peak at 3396 cm^{-1} [34]. The marked broadness of the peak of the OH groups is due to the hydrogen bonds that are produced by the interlayered carbonate anions and water molecules [23,35]. These hydrogen bonds were marked by a weak shoulder at 2923 cm^{-1} [1,19,20].

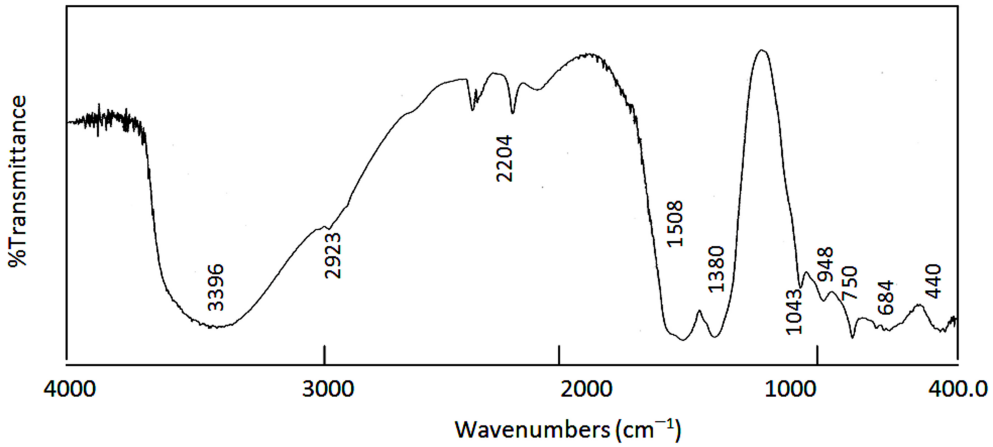

Figure 6. Fourier transform infrared spectrum of Ni–Zn–Ti LDH.

A weak peak was detected at 2204 cm^{-1}, demonstrating the presence of cyanate anions as secondary anions [1,35]. Additionally, the strong peaks at 1508 cm^{-1} and 1380 cm^{-1} indicated that the carbonate anions are the main interlayered anions inside the LDHs. These strong bands correspond with the vibrational mode of CO_3 [28,29]. However, the actual band of the free molecules of CO_3 was reported in previous studies occurring at 1450 cm^{-1}. By lowering the symmetry, the split and separation of this band occurred in a similar manner to the two bands of aragonite, which were previously reported to occur at 1504 cm^{-1} and 1492 cm^{-1} [1,19]. The other vibrational modes (ν_1 and ν_2) of carbonate, which were recorded at 1043 cm^{-1} and 948 cm^{-1}, respectively, indicated the existence of carbonates inside the LDHs as the main anions [29]. The vibrational modes of metal–oxygen, which belong to Ni–O, Zn–O, and Ti–O, were observed in the range of 800 cm^{-1} to 400 cm^{-1} [29,35]. These results suggest that the Ni-Zn-Ti LDH consists of two interlayered anions, with carbonate as the main anion and cyanate as the secondary anion in addition to the hydroxyl groups and a small quantity of water.

It is known that a platy structure is the most common morphology for nanolayered structures, which are produced by building LDHs [1–3]. Scanning electron microscopy produced the images of the Ni–Zn–Ti LDH shown in Figure S1. During the imaging process, an ultra-thin layer of platinum was used as a cover for the measured samples. The function of the platinum layers involves increasing the resolution of the SEM images. Figure S1 shows clear plates with irregular shapes. In addition, Figure S1a,b reveal that Ni–Zn–Ti LDH consists of aggregates of small and fine plates. Via magnification, Figure S1c,d indicate that the platelets of Ni–Zn–Ti LDH are in the nanoscale.

Figure S2 shows the SEM images of the morphology of the Ni–Zn–Ti LDHs after calcination at 500 °C. Figure S2a indicates that the thermal treatment created nanoparticles and nanopores inside the nanolayers of multi-oxides of Ni–Zn–Ti by releasing carbon dioxide gases and water vapor from the thermal decomposition of the anions. Using magnification, nanopores were observed and are marked by arrows in Figure S2b. Additionally, Figure S2b shows that the Ni–Zn–Ti–500 has nanoparticles smaller than 50 nm.

The different elements of Ni–Zn–Ti–500 were identified using EDX analysis. Figure S2c shows clear peaks in the spectrum of Ni–Zn–Ti–500 for zinc, nickel, and titanium. The high percentages of oxygen and zinc, which were 48.96% and 39.58%, respectively, indicate that this sample has a ZnO structure. At the same time, the low percentages of nickel and titanium confirmed the formation of the dual Ni/Ti-doped zinc oxide for the Ni–Zn–Ti–500 sample, a finding that agrees with the XRD results.

This finding was confirmed by the SEM images of Ni–Zn–Ti after the thermal treatment at 900 °C. Figure S3a,b show that the nanoparticles started to blend and recrystallize at this high temperature. Therefore, large and small particles can be observed in Figure S3a,b. Additionally, the formation of the dual Ni/Ti-doped zinc oxides was confirmed by the EDX

spectrum, as shown in Figure S3c, where the high percentages are due to zinc and oxygen. In addition, low percentages are recorded for both nickel and titanium.

2.2. Optical Properties

The oxide forms of nickel, zinc, and titanium are the most prolific materials in the field of optical applications. Therefore, the optical parameters of their nanolayers and nanocomposites are discussed in detail based on the measurement of UV–Vis absorbance spectroscopy. For comparison, the UV–Vis absorbance of the conventional nanolayered structures of the Al–Zn LDHs was measured and is displayed in Figure 7a (inset). There is no absorbance in the UV region for the Al–Zn LDHs. In the case of the Ni–Zn–Ti LDHs, the spectrum of UV–Vis absorbance showed three maxima at 400 nm, 220 nm, and 200 nm, as shown in Figure 7a. The comparison between the spectra of the Ni–Zn–Ti LDHs and Zn–Al LDHs indicates that there is an obvious absorbance in the UV region, shifting near to the visible area for the Ni–Zn–Ti LDHs. This means that the optical behavior of the LDH was boosted by the integration of nickel and titanium with zinc oxides.

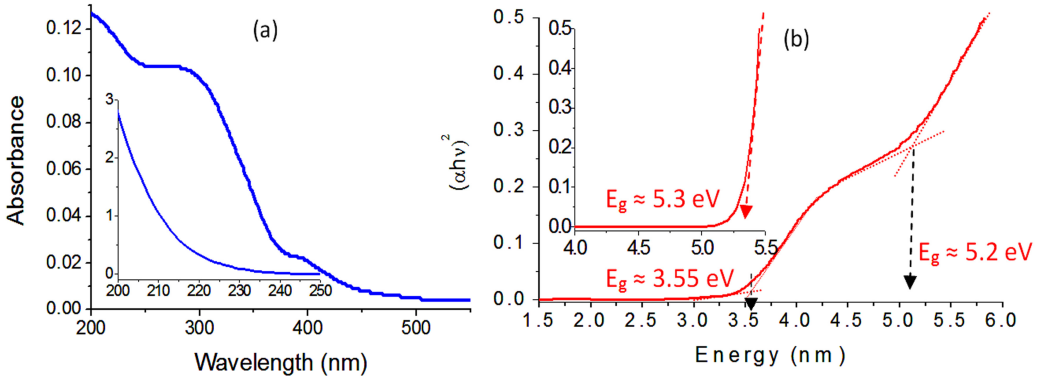

Figure 7. The sample Ni–Zn–Ti LDHs (inset-, Zn–Al LDHs): (**a**) absorbance spectra and (**b**) energy of the band gap.

The band gap energy is one of the most important parameters when measuring the photoactivity of the prepared materials. The band gap energy was calculated according to the relation between the exposed energy (hν) and the absorbance factor of the Ni–Zn–Ti LDHs, as shown in the following scientific formula [36]:

$$(\alpha h\nu)^2 = \text{constant}\ (h\nu - E_g)$$

where (h) is Planck's constant. The light velocity (3×10^8 m/s) and the absorbance wavelength are used to calculate the frequency of light (ν). The absorbance coefficient of the prepared materials is α. When plotting the value $(\alpha h\nu)^2$ along the Y-axis and the energy (hν) along the X-axis, the band gap energy can be calculated by extending a straight line toward the X-axis. At $(\alpha h\nu)^2$ = zero, the band gap energy equals the incident photon energy. Figure 7b shows the band gap energy of both the conventional Al–Zn LDHs and Ni–Zn–Ti LDHs. Additionally, the calculated band gap energies of the prepared materials are summarized in Table 2.

Table 2. The band gap energy of the prepared materials.

Samples	Band Gap Energy (eV)
Zn–Al LDH	5.3
Zn–Al–500	3.25
Ni–Zn–Ti LDH	5.2 and 3.55
Ni–Zn–Ti–500	3.11
Ni–Zn–Ti–900	3.05

Figure 7b shows that the Ni–Zn–Ti LDHs have two band gap energies. These band gap energies are observed at 5.2 eV and 3.55 eV. By conducting a comparison with the band gap energy of the Al–Zn LDHs, which is shown in Figure 7b (inset) and Table 2, the energy of the band gap can be seen to have shifted from 5.30 eV to lower values of 3.55 eV and 5.2 eV for the Ni–Zn–Ti LDHs. This lower shift confirmed that the integration of nickel with titanium inside the LDHs' layers boosted the optical behavior of the layered structures of the LDHs. This improvement extended to the multi-oxides form, which was produced from the calcination of these nanolayered structures.

Due to the calcination of the LDHs at 500 °C and 900 °C, new optical materials were observed, as shown in Figure 8. For the Ni–Zn–Ti–500 sample, Figure 8a,b show a maximum at 400 nm and two weak maxima at 500 nm and 650 nm. Similar results were observed for the Ni–Zn–Ti–900 sample, which exhibited a strong maximum at 400 nm in addition to the two weak maxima. Compared with the doped zinc oxide Zn–Al–500 (Figure 8c), the absorbance edge of nanocomposites Ni–Zn–Ti–500 and Ni–Zn–Ti–900 shifted toward a higher wavelength, as shown in Figure 8a,b. This shift indicates an improvement in the optical behavior of the Ni–Zn–Ti nanocomposites compared with the zinc oxide based on the normal Al–Zn LDHs. This improvement was also observed by determining the energy of the band gap. Figure 8d and Table 2 show that the Ni–Zn–Ti–500 sample has lower band gap energy than doped zinc oxide Al–Zn–500; the band gap energy of Ni–Zn–Ti–500 was 3.1 eV, as shown in Figure 8d. This improvement extended to the band gap energy of Ni–Zn–Ti–900. Figure 8e shows that it has a band gap energy of 3.05 eV. When comparing it with the band gap energy of the Zn–Al–500 nanoparticles (Figure 8f), the dual Ni/Ti doping process for zinc oxides decreased the energy of the band gap from 3.25 eV to 3.05–3.10 eV, as shown in Table 2. Compared with the pure zinc oxide (3.2 eV) or pure titanium oxide (3.3 eV), the combination of them when also inserting nickel led to a reduction in the energy (3.05–3.10 eV). This reduction in the band gap energy and the shift in the absorbance of the Ni/Ti/Zn oxides nanocomposites toward a higher wavelength improved the optical properties of the zinc oxide, increasing its optical applications and activity.

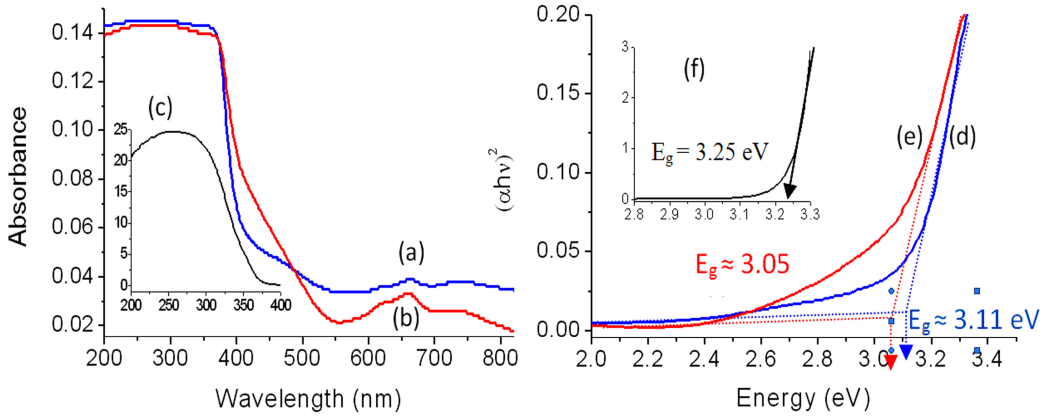

Figure 8. Absorbance spectra of the Ni–Zn –Ti LDHs at (**a**) 500 °C and (**b**) 900 °C. (**c**) Absorbance spectrum of the normal Zn–Al LDHs at 500 °C. The band gap energy of the Ni–Zn–Ti LDHs after calcination at (**d**) 500 °C and (**e**) 900 °C. (**f**) The band gap energy of the normal Zn–Al LDHs at 500 °C.

2.3. Photocatalytic Degradation of Green Dyes

Photoactive materials are useful for removing industrial pollutants through photocatalytic decomposition using light [37–45]. Thus, the photocatalytic decomposition of green dyes was studied in the presence of UV light using the layered structures of Ni–Zn–Ti LDHs and the dual Ni/Ti-doped zinc oxide nanocomposites as photocatalysts. Moreover, in addition to the pure zinc oxide, the photocatalytic activities of the conventional Al–Zn LDHs and the Al-doped zinc oxide were measured using the same reaction for comparison.

To track the dye concentration, an appropriate amount of liquid was withdrawn after the radiation of the UV light for a few minutes, and its absorbance was measured using a

UV–Vis spectrophotometer. The gradual decrease in the characteristic peak of the dye at 714 nm indicated the decomposition of the main structure of the pollutants. We tracked the reduction in the other peaks at 320 nm, 283 nm, and 232 nm, and the complete degradation of the internal parts of the dye is shown in Figure 9a–c.

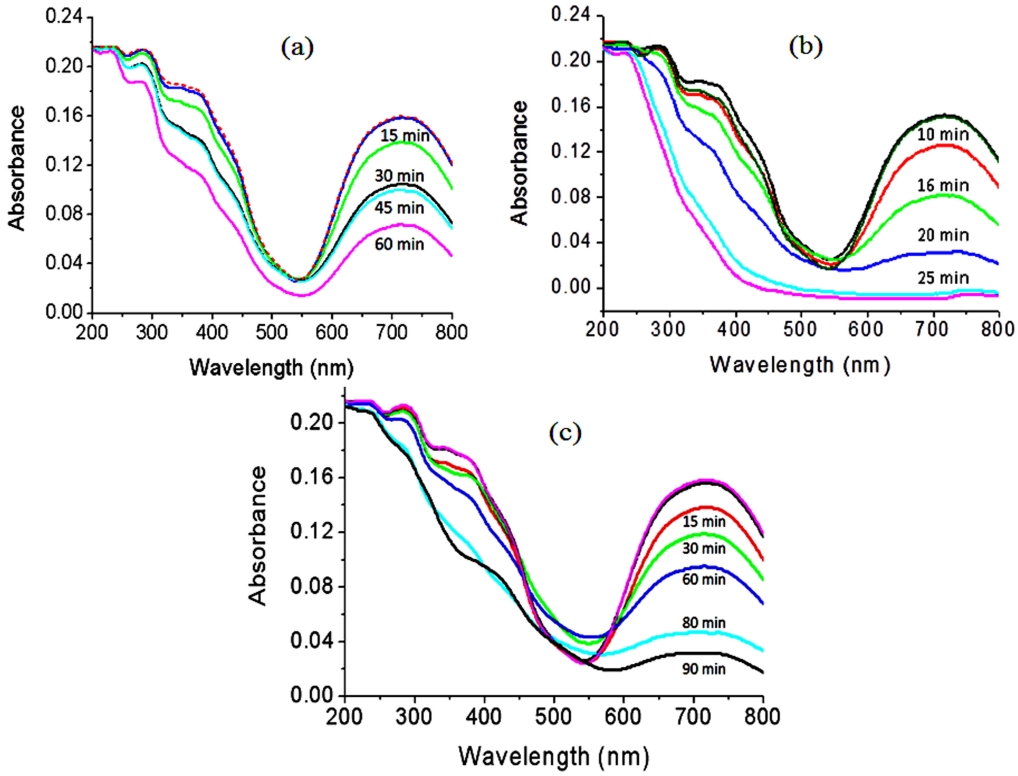

Figure 9. UV–Vis absorption spectra of the dyes with (**a**) Ni–Zn–Ti LDH after a period of irradiation, (**b**) Ni–Zn–Ti–500 after a period of irradiation, and (**c**) Ni–Zn–Ti–900 after a period of irradiation.

Using a blank test (without a photocatalyst), the stability of the green dye was observed with the irradiation of the UV light. The photocatalytic decomposition of the green dye and the radiation time of the UV light were studied to determine the photoactivity of the prepared photocatalysts. When the green solution of the dye was stirred with the photocatalyst in the dark, the concentration of the dye did not change over the one hour the experiment was conducted without light. In the presence of UV light, the photocatalytic decomposition of the green dye was observed via the gradual disappearance of the green color of the industrial pollutant. The obtained results are illustrated in Figure 9a–c.

The photocatalytic decomposition of AG1 in the presence of UV light and the Ni–Zn–Ti LDH increased as the radiation time increased. After 60 min, the degradation of the green dye was 55.6%, as shown in Figure 9a. When using Ni–Zn–Ti–500, the percentage of decomposition reached 100% after 25 min, as shown in Figure 9b. The complete disappearance of the green dyes indicates that the dual Ni/Ti-doped zinc oxides nanocomposite became more effective in the presence of UV light. Meanwhile, the Ni–Zn–Ti–900 sample could not completely remove the green dye until it had undergone 90 min of UV-light radiation, as shown in Figure 9c.

For the Al-doped zinc oxide, the photocatalyst Al/Zn-500 caused the full degradation of the dye after 155 min of UV-light radiation. The comparison of the Al-doped zinc oxide and the dual Ni/Ti-doped zinc oxide indicated the strong effect of the dual dopants of both nickel and titanium on the photoactivity of ZnO. In addition, the pure zinc oxide showed 100% degradation for the same dyes after 51 min of UV radiation. This means that the presence of two dopants, Ni and Ti, improved the photoactivity of ZnO, enabling the full decomposition of the green dye in a shorter time.

2.4. Kinetic Study of the Photocatalytic Degradation of Green Dyes

The kinetic reactions of the degradation process of the AG1 dye were studied using the following formula:

$$\ln C_o/C = kt$$

The concentration of the dyes (C_o) was measured at a time of zero. The concentration of the dyes (C) was then determined at different times. The value (k) is the rate constant of the reaction. The kinetic plots of the photocatalytic decomposition of the dye using the layered materials of the Ni–Ti–Zn LDHs and the dual Ni/Ti-doped zinc oxides are displayed in Figure 10.

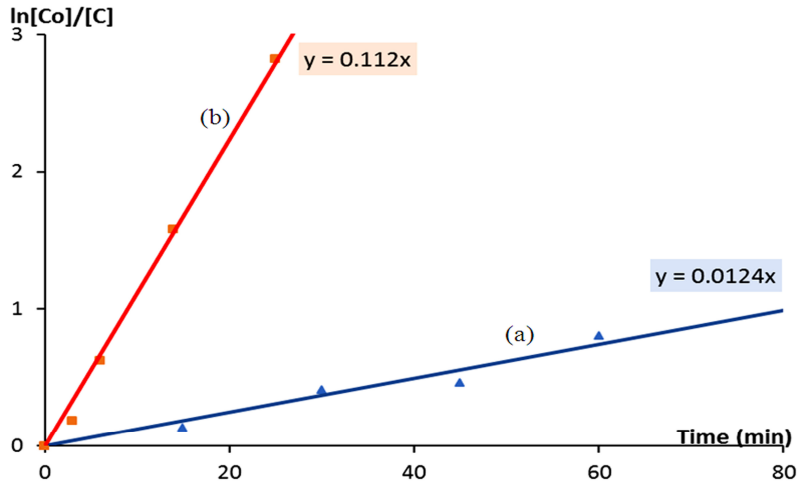

Figure 10. The rate of the photocatalytic decomposition reaction of the dye in the presence of light and (**a**) Ni–Zn–Ti LDHs and (**b**) Ni–Zn–Ti–500.

Figure 10a shows the linear relation of the decomposition of the dyes using the layered structure of the Ni–Ti–Zn LDHs. This linear relation means that this process is a pseudo-first-order kinetic reaction. It is known that a pseudo-first-order reaction is a bimolecular reaction that appears like a first-order reaction (monomolecular reaction) due to more concentration of one reactant than the other reactant. In the current reaction, the concentration of water is constant during the reaction. At the same time, the concentration of the dye strongly changed with time during the reaction. Therefore, the decomposition of the dye belongs to a pseudo-first-order reaction. Additionally, Figure 10a shows that the rate constant of the reaction is 0.012 min^{-1}. The linear relation of the decomposition reaction of the dyes using the multi-doped zinc oxide Ni–Zn–Ti–500 is displayed in Figure 10b. The rate constant of the decomposition reaction was found to be 0.112 min^{-1}. The comparison between the Ni–Ti–Zn LDH and its nanocomposite Ni–Zn–Ti–500 indicated that the dual Ni/Ti-doped zinc oxides accelerated the rate reactions of the photocatalytic decomposition of the green dyes ten times faster than the Ni–Ti–Zn LDHs.

3. Discussion

The full degradation and decolorization of the green dyes were achieved in a short period of light radiation by the multi-doped Ni–Ti–ZnO. During 25 min of light radiation, the green color of the dyes disappeared; additionally, the absorbance peak of the dyes at 714 nm disappeared, as shown in Figure 9b. This means that the main skeleton of these organic pollutants was completely oxidized, becoming carbon dioxide and water. This finding was confirmed by the disappearance of the other bands of these pollutants at 320 nm, 283 nm, and 232 nm because these peaks are attributed to organic phenyl groups.

Photocatalysis processes depend on the production of strong oxidizing agents from photoactive materials using light. These oxidizing agents play a key role in decomposing and removing organic pollutants. The mechanism of photoactive materials mainly involves

the excitation of their electrons by photons of light, enabling their separation and jumping to the conduction band. In this way, holes start to grow in the valance band. The superoxide radicals $^{\bullet}O_2^-$ are produced when excited electrons react with oxygen molecules. These radicals are strong oxidizing agents. In addition, other oxidizing agents are formed from the reaction between the holes and water molecules, forming hydroxide radicals. The $^{\bullet}$OH radicals are highly oxidizing agents.

By accelerating the mechanism of the photoactive materials, high levels of photocatalytic activity were achieved with the Ni–Zn–Ti–500 multi-doped zinc oxides. Three factors enabled the mechanism of the photoactivity of the multi-doped ZnO to be accelerated. The small nanosize of Ni–Zn–Ti–500 is the first factor; such nanosizes generate new photoactive centers. The lowering of the band gap energy is the second factor. The reduction from 3.25 eV to 3.10 eV led to the acceleration of the separation stage to increase the number of electrons in the conduction band and the number of holes in the valance band. The third factor relates to the porous structure of Ni–Zn–Ti–500. This porous structure trapped and confined the pollutants inside the photocatalyst. These three parameters are the driving force behind the high photocatalytic activity of Ni–Zn–Ti–500 and the improved photocatalytic degradation of the dyes.

For Ni–Zn–Ti–900, the photoactivity decreased, reducing the photocatalytic degradation of the dyes. These results can be explained through the same three factors. The first factor was nullified because the Ni–Zn–Ti–900 lost its nanostructure and converted to a microscale, as shown in the SEM images. The high temperature (900 °C) caused the blocking of the photoactive sites in the structure of the photocatalyst through the sintering process. Additionally, the third factor was cancelled out because the SEM images showed the disappearance of the porous structure of the photocatalyst. This means that two of the three key factors failed to activate the Ni–Zn–Ti–900 sample, preventing it from decomposing the pollutants.

In the case of the Ni–Ti–Zn LDHs, the low levels of photoactivity are due to the failure of the second factor. The large band gap energy of the Ni–Ti–Zn LDHs led to weak separation processes between the electrons and holes because higher levels of energy (more than 3.5 eV and 4.2 eV) needed to be absorbed to excite the electron to jump to the conduction bands.

This explanation was confirmed by the kinetic study. For the nanolayers of Ni–Zn –Ti LDHs, the rate of the photocatalytic reaction of the green dyes was 0.0124 min^{-1}. Using the multi-doped ZnO (Ni–Zn–Ti–500), the rate of the photocatalytic reaction with the green dyes increased ten times, reaching a value of 0.112 min^{-1}.

4. Conclusions

In this study, the nanolayered structures of a ternary system were successfully produced for nickel, titanium, and zinc. At the same time, multiple objectives were achieved by converting the prepared Ni–Ti–Zn nanolayered structures to organic–inorganic nanohybrids and nanocomposites. Initially, two groups of Ni–Ti–Zn–organic nanohybrids were prepared for the first time. Via host–guest interactions, the nanolayers of the Ni–Ti–Zn were combined with long chains of hydrocarbons to form organic–inorganic nanohybrids. We then focused on producing a highly optically active nanocomposite. Using a thermal treatment, the prepared two-dimensional nanolayers were converted into three-dimensional nanocomposites based on the multi-doped Ni/Ti–zinc oxides. The positive effect of the dual dopants of both nickel and titanium decreased the band gap energy of the zinc oxide to 3.1 eV, producing a highly optically active nanomaterial. Finally, we purified water containing organic pollutants in 25 min of light radiation. This achievement was attained using the multi-doped Ni/Ti–zinc oxide nanocomposite by accelerating the photocatalytic decomposition of the pollutants of the industrial dye. These positive results could lead to the development of new nanohybrids based on multi-metals and organic compounds. At the same time, the present study suggests a novel method for fabricating photoactive nanocomposites for water purification and environmental remediation.

5. Materials and Methods

5.1. Design of a Tripartite System of Nanolayered Materials

Urea hydrolysis was used to prepare the tripartite system of layered zinc–titanium–nickel double hydroxides. In these hydrolysis reactions, cyanate and carbonate anions were produced from the thermal decomposition of urea at 80 °C. At the same time, the acidic environment of the reaction was changed to an alkaline medium from pH = 3.2 to pH = 8.2. This change enabled the formation of cationic nanolayers containing zinc, titanium, and nickel. These conditions are suitable for designing a tripartite system of nanolayered structures. The cationic nanolayers can act as roofs and the anionic compounds can work as pillars when designing the tripartite system of nanolayered materials. Practically, the aqueous mixture of zinc chloride (4.95×10^{-2} M), nickel chloride hexahydrate (9.95×10^{-3} M), and titanium chloride (9.95×10^{-3} M) was reacted with the aqueous solution of urea. The concentration of urea was 0.5 M. This reaction was completed by heating and stirring for 12 h at 80 °C. After the filtration, washing, and separation processes were carried out, the product was dried in a vacuum at room temperature for 24 h. The Zn–Al LDH used for comparison was synthesized under the same conditions. The nanocomposites were prepared through the calcination of the prepared materials at 500 °C and 900 °C for 6 h in air.

5.2. Design of Ni–Zn–Ti–Organic Nanohybrids

The nanolayered structure of Ni–Zn–Ti LDH was not clear. In order to clarify the crystalline structure of the nanolayered structures, long chains of hydrocarbons intercalated between the nanolayers looking like pillars to widen the interlayered space among the cationic nanolayers through host–guest interaction. The host is Ni–Zn–Ti LDH and the guest is the organic compounds. In this trend, two series of organic compounds were used to design Ni–Zn–Ti–organic nanohybrids. The first series was based on stearic acid sodium salt $C_{17}H_{35}COONa$, myristic acid sodium salt $C_{13}H_{27}COONa$, and *n*-capric acid sodium salt $C_9H_{19}COONa$. The second series was based on sebacic acid sodium salt $COOHC_8H_{16}COOH$ and suberic acid sodium salt $COOHC_6H_{12}COOH$. Due to the anion exchange property of the layered double hydroxides, different kinds of Ni–Zn–Ti–organic nanohybrids were formed. In practical terms, an appropriate amount of the sodium salt of organic acid (2×10^{-3} mol) was dissolved in 10 mL of water to obtain 0.2 M of an aqueous solution of organic species. At the same time, fine particles of LDH (0.5 g) were suspended in the aqueous solution of organic species using the ultrasonic technique. The intercalation reactions were carried out in the presence of an inert gas via stirring for 6 h at 60 °C. After the filtration, washing, and separation processes were completed, the product was dried in a vacuum at room temperature.

5.3. Characterization of the Prepared Samples

In order to identify the texture of the nanohybrids, nanolayered structures, and nanocomposites, a Rigaku RINT 2200 (Rigaku, Tokyo, Japan), with Cu Kα (filtered) radiation (λ= 0.154 nm) was used to measure the X-ray diffraction between the angles 2Θ = 1.8–50° within step of 0.02° and step time 0.4 s. Scanning electron microscopy (JSM–6330F, JEOL, Tokyo, Japan) was used to image the prepared products. EDX was used to detect the different elements in the prepared nanomaterials. The thermal analyses were performed using a SSC5200, Seiko, Tokyo, Japan. The curves of the thermal gravimetric analysis (TGA) and differential thermal gravimetric (DTG) analysis were produced by heating the prepared samples up to 800 °C at 10 °C/min in air. The same apparatus was used to conduct the differential thermal analysis (DTA) under the same conditions. A Horiba FT–720 apparatus (Horiba, Tokyo, Japan) was used to detect the functional groups in the wide range of wavenumbers 425–4000 cm^{-1} using Fourier transform infrared (FT–IR) spectroscopy. The optical parameters of the solid photocatalysts were measured using the diffuse reflectance technique through the integrating sphere (ISR–603) with a Shimadzu 3600 spectrophotometer (Shimadzu, Columbia, MD, USA). The optical absorbance of the

liquid samples was determined using the conventional technique with a UV–VIS–IR–3600 Shimadzu (Shimadzu, Columbia, MD, USA).

5.4. Photocatalytic Processes

The photocatalytic decomposition of the green dyes was carried out to determine the photocatalytic activities of the prepared nanostructures. An immersion well reactor RQ400 (Camberley, Surrey, UK) was used to perform photocatalytic processes. The immersed lamps are designed to ensure good contact between the lamps and the solutions, enabling effective photochemical processes. Additionally, a cooling system for the immersed lamps was used to prevent thermal reactions. The medium pressure of the mercury lamp (400 W) is suitable for photochemical presses because it produces a wide range of wavelengths in the UV and visible spectra. A 400 mL flask was used to carry out the photocatalytic reactions in the polluted water with Acid Green 1 dyes. A low concentration of the green dye was prepared as an aqueous solution with 4×10^{-4} M. By determining the absorbance at the characteristic band of the dyes (714 nm), the concentration of the pollutants can be measured according to the Beer and Lambert equation. In order to account for other factors, such as the processes of adsorption, absorption, and photolysis, two blank experiments were carried out: one without photocatalysts and another without light. The routine experiment involved withdrawing a small amount of the solution after irradiation with UV light at different time intervals. After that, a UV–Vis spectrophotometer was used to measure and chart the concentration of the dyes.

Supplementary Materials: The following supporting information can be downloaded at: https://www.mdpi.com/article/10.3390/catal14060340/s1, Figure S1: Scanning electron microscopy images of Ni–Zn–Ti LDH at: (a) at location in the micro scale, (b) the other location in the micro scale, (c) at location in the nano scale and (d) the other location in the nano scale.; Figure S2: SEM images of Ni–Zn–Ti LDH after thermal treatment at 500 °C (a) 1 µm, (b) 50 nm and (c) EDX analysis; Figure S3: SEM image of the Ni–Zn–Ti LDHs after thermal treatment at 900 °C (a) 100 nm, (b) 100 nm after magnification and (c) EDX analysis.

Author Contributions: Conceptualization, O.S.; methodology, O.S., M.O. and A.O.; software, A.O.; validation, O.S. and M.O.; formal analysis, N.M.S. and O.S.; investigation, A.O., O.S., M.O. and N.M.S.; resources, M.O., O.S. and A.O.; data curation, A.O. and M.O.; writing—original draft preparation, M.O., A.O. and O.S.; writing—review and editing, O.S. and N.M.S.; visualization, O.S. and M.O.; supervision, O.S. and A.O.; project administration, O.S.; funding acquisition, O.S. All authors have read and agreed to the published version of the manuscript.

Funding: This work was funded by the Deputyship for Research & Innovation, Ministry of Education in Saudi Arabia under grant no. INST221, and The APC was funded by the same grant, INST221.

Data Availability Statement: Data will be provided by the authors upon request.

Acknowledgments: The authors extend their appreciation to the Deputyship for Research & Innovation, Ministry of Education in Saudi Arabia for funding this research work through project number INST221.

Conflicts of Interest: The authors declare no conflicts of interest.

References

1. Saber, O.; Osama, A.; Alshoaibi, A.; Shaalan, N.M.; Osama, D. New Approach for Designing Zinc Oxide Nanohybrids to Be Effective Photocatalysts for Water Purification in Sunlight. *Nanomaterials* **2022**, *12*, 2005. [CrossRef] [PubMed]
2. Saber, O.; Osama, A.; Alshoaibi, A.; Shaalan, N.M.; Osama, D. Designing inorganic–magnetic–organic nanohybrids for producing effective photocatalysts for the purification of water. *RSC Adv.* **2022**, *12*, 18282–18295. [CrossRef] [PubMed]
3. Ljubas, D.; Juretić, H.; Badrov, A.; Biošić, M.; Babić, S. Photocatalytic Degradation of Pharmaceutical Trimethoprim in Aqueous Solution over Nanostructured TiO_2 Film Irradiated with Simulated Solar Radiation. *Appl. Sci.* **2023**, *13*, 5681. [CrossRef]
4. Xu, S.M.; Pan, T.; Dou, Y.B.; Yan, H.; Zhang, S.T.; Ning, F.Y.; Shi, W.Y.; Wei, M. Theoretical and experimental study on (MMIII)-M-II-layered double hydroxides as efficient photocatalysts toward oxygen evolution from water. *J. Phys. Chem. C* **2015**, *119*, 18823–18834. [CrossRef]

5. Gholami, P.; Khataee, A.; Soltani, R.D.C.; Dinpazhoh, L.; Bhatnagar, A. Photocatalytic degradation of gemifloxacin antibiotic using Zn-Co-LDH@biochar nanocomposite. *J. Hazard. Mater.* **2020**, *382*, 121070. [CrossRef] [PubMed]
6. Xiong, X.Y.; Zhao, Y.F.; Shi, R.; Yin, W.J.; Zhao, Y.X.; Waterhouse, G.I.N.; Zhang, T.R. Selective photocatalytic CO_2 reduction over Zn-based layered double hydroxides containing tri or tetravalent metals. *Sci. Bull.* **2020**, *65*, 987–994. [CrossRef] [PubMed]
7. Parida, K.M.; Mohapatra, L. Carbonate intercalated Zn/Fe layered double hydroxide: A novel photocatalyst for the enhanced photo degradation of azo dyes. *Chem. Eng. J.* **2012**, *179*, 131–139. [CrossRef]
8. Bouaziz, Z.; Soussan, L.; Janot, J.-M.; Jaber, M.; Amara, A.B.H.; Balme, S. Dual role of layered double hydroxide nanocomposites on antibacterial activity and degradation of tetracycline and oxytetracyline. *Chemosphere* **2018**, *206*, 175–183. [CrossRef] [PubMed]
9. Liu, J.; Wu, P.; Li, S.; Chen, M.; Cai, W.; Zou, D.; Zhu, N.; Dang, Z. Synergistic deep removal of As(III) and Cd(II) by a calcined multifunctional MgZnFe-CO_3 layered double hydroxide: Photooxidation, precipitation and adsorption. *Chemosphere* **2019**, *225*, 115–125. [CrossRef] [PubMed]
10. Yuan, X.; Li, W. Graphitic-C3N4 modified ZnAl-layered double hydroxides for enhanced photocatalytic removal of organic dye. *Appl. Clay Sci.* **2017**, *138*, 107–113. [CrossRef]
11. Yang, Y.; Li, J.; Yan, T.; Zhu, R.; Yan, L.; Pei, Z. Adsorption and photocatalytic reduction of aqueous Cr(VI) by Fe3O4-ZnAl-layered double hydroxide/TiO2 composites. *J. Colloid Interface Sci.* **2020**, *562*, 493–501. [CrossRef] [PubMed]
12. Yang, Y.Q.; Zheng, Z.H.; Yang, M.H.; Chen, J.F.; Li, C.; Zhang, C.H.; Zhang, X.D. In-situ fabrication of a spherical-shaped Zn-Al hydrotalcite with BiOCl and study on its enhanced photocatalytic mechanism for perfluorooctanoic acid removal performed with a response surface methodology. *J. Hazard. Mater.* **2020**, *399*, 123070. [CrossRef] [PubMed]
13. Li, J.; Xu, Y.; Ding, Z.; Mahadi, A.H.; Zhao, Y.; Song, Y.-F. Photocatalytic selective oxidation of benzene to phenol in water over layered double hydroxide: A thermodynamic and kinetic perspective. *Chem. Eng. J.* **2020**, *388*, 124248. [CrossRef]
14. Ye, J.; Liu, J.; Huang, Z.; Wu, S.; Dai, X.; Zhang, L.; Cui, L. Effect of reduced graphene oxide doping on photocatalytic reduction of Cr(VI) and photocatalytic oxidation of tetracycline by ZnAlTi layered double oxides under visible light. *Chemosphere* **2019**, *227*, 505–513. [CrossRef] [PubMed]
15. Wang, L.; Zhu, Z.; Wang, F.; Qi, Y.; Zhang, W.; Wang, C. State-of-the-art and prospects of Zn-containing layered double hydroxides (Zn-LDH)-based materials for photocatalytic water remediation. *Chemosphere* **2021**, *278*, 130367. [CrossRef]
16. Mohapatra, L.; Parida, K. A review on the recent progress, challenges and perspective of layered double hydroxides as promising photocatalysts. *J. Mater. Chem.* **2016**, *4*, 10744–10766. [CrossRef]
17. Xu, M.; Bi, B.; Xu, B.; Sun, Z.; Xu, L. Polyoxometalate-intercalated ZnAlFelayered double hydroxides for adsorbing removal and photocatalytic degradation of cationic dye. *Appl. Clay Sci.* **2018**, *157*, 86–91. [CrossRef]
18. Shao, M.; Han, J.; Wei, M.; Evans, G.D.; Duan, X. The synthesis of hierarchical Zn–Ti layered double hydroxide for efficient visible-light photocatalysis. *Chem. Eng. J.* **2011**, *168*, 519–524. [CrossRef]
19. Xia, S.-J.; Liu, F.-X.; Ni, Z.M.; Xue, J.-L.; Qian, P.-P. Layered double hydroxides as efficient photocatalysts for visible-light degradation of Rhodamine B. *J. Colloid Interface Sci.* **2013**, *405*, 195–200. [CrossRef]
20. Chowdhury, P.R.; Bhattacharyya, K.G. Ni/Ti layered double hydroxide: Synthesis, characterization and application as a photocatalyst for visible light degradation of aqueous methylene blue. *Dalton Trans.* **2015**, *44*, 6809–6824. [CrossRef]
21. Parida, K.; Mohapatra, L. Recent progress in the development of carbonate-intercalated Zn/Cr LDH as a novel photocatalyst for hydrogen evolution aimed at the utilization of solar light. *Dalton Trans.* **2012**, *41*, 1173–1178. [CrossRef] [PubMed]
22. Zhao, Y.; Zhang, S.; Li, B.; Yan, H.; He, S.; Tian, L.; Shi, W.; Ma, J.; Wei, M.; Evans, D.G.; et al. A Family of Visible-Light Responsive Photocatalysts Obtained by Dispersing CrO6 Octahedra into a Hydrotalcite Matrix. *Chem.—Eur. J.* **2011**, *17*, 13175–13181. [CrossRef] [PubMed]
23. Cao, Y.; Gou, H.; Zhu, P.; Jin, Z. Ingenious Design of CoAl-LDH p-n Heterojunction Based on CuI as Holes Receptor for Photocatalytic Hydrogen Evolution, Chinese Journal of Structural Chemistry. *Chin. J. Struct. Chem.* **2022**, *41*, 2206079.
24. Han, G.; Xu, F.; Cheng, B.; Li, Y.; Yu, J.; Zhang, L. Enhanced Photocatalytic H_2O_2 Production over Inverse Opal ZnO@ Polydopamine S-Scheme Heterojunctions. *Acta Phys.—Chim. Sin.* **2022**, *38*, 2112037–2112047. [CrossRef]
25. Long, X.; Meng, J.; Gu, J.; Ling, L.; Li, Q.; Liu, N.; Wang, K.; Li, Z. Interfacial Engineering of NiFeP/NiFe-LDH Heterojunction for Efficient Overall Water Splitting. *Chin. J. Struct. Chem.* **2022**, *41*, 2204046–2204053.
26. Baran, T. Efficiency of volatile organic compound degradation in air using doped strontium titanate photocatalysts. Quenching experiments towards understanding of doping mechanisms. *React. Kinet. Mech. Catal.* **2023**, *136*, 3243–3256. [CrossRef]
27. Constantino, V.R.L.; Pinnavaia, T. Basic properties of $Mg^{2+}{}_{1-x}Al^{3+}{}_x$ layered double hydroxides intercalated by carbonate, hydroxide, chloride, and sulfate anions. *Inorg. Chem.* **1995**, *34*, 883. [CrossRef]
28. Yun, S.; Pinnavaia, T. Water content and particle texture of synthetic hydrotalcite-like layered double hydroxides. *Chem. Mater.* **1995**, *7*, 348–354. [CrossRef]
29. Saber, O.; Tagaya, H. New layered double hydroxide, Zn–Ti LDH: Preparation and intercalation reactions. *J. Incl. Phenom. Macrocycl. Chem.* **2003**, *45*, 109–116. [CrossRef]
30. Saber, O.; Tagaya, H. Preparation and intercalation reactions of nano-structural materials, Zn–Al–Ti LDH. *Mater. Chem. Phys.* **2008**, *108*, 449–455. [CrossRef]
31. Saber, O.; Tagaya, H. Preparation and intercalation reactions of Zn-Sn LDH and Zn-Al-Sn LDH. *J. Porous Mater.* **2003**, *10*, 83–91. [CrossRef]

32. Saber, O.; Tagaya, H. Preparation of a new nano-layered materials and organic–inorganic nano-hybrid materials, Zn–Si LDH. *J. Porous Mater.* **2009**, *16*, 81–89. [CrossRef]
33. Muramatsu, K.; Saber, O.; Tagaya, H. Preparation of new layered double hydroxide, Zn-Mo LDH. *J. Porous Mater.* **2007**, *14*, 481–484. [CrossRef]
34. Saber, O.; Ansari, S.A.; Parveen, N.; Shaalan, N.M.; Osama, A.; Osama, M. Positive Influence of Oxalate and Cyanate on the Supercapacitance Performance of V/Co 2D-Nanolayered Structures. *Inorganics* **2023**, *11*, 458. [CrossRef]
35. Nakamoto, N. *Infrared and Raman Spectra of Inorganic and Coordination Compounds*, 4th ed.; Wiley: New York, NY, USA, 1986.
36. Makuła, P.; Pacia, M.; Macyk, W. How To Correctly Determine the Band Gap Energy of Modified Semiconductor Photocatalysts Based on UV–Vis Spectra. *J. Phys. Chem. Lett.* **2018**, *9*, 6814–6817. [CrossRef] [PubMed]
37. Mugumo, R.; Ichipi, E.; Tichapondwa, S.M.; Chirwa, E.M.N. Visible-Light-Induced Photocatalytic Degradation of Rhodamine B Dye Using a CuS/ZnS p-n Heterojunction Nanocomposite under Visible-Light irradiation. *Catalysts* **2023**, *13*, 1184. [CrossRef]
38. Zhu, J.; Zhu, Y.; Zhou, Y.; Wu, C.; Chen, Z.; Chen, G. Synergistic Promotion of Photocatalytic Degradation of Methyl Orange by Fluorine- and Silicon-Doped TiO_2/AC Composite Material. *Molecules* **2023**, *28*, 5170. [CrossRef] [PubMed]
39. Elamin, M.R.; Abdulkhair, B.Y.; Elamin, N.Y.; Ibnaouf, K.H.; Idriss, H.; Bakheit, R.; Modwi, A. Application of Synthesized Vanadium–Titanium Oxide Nanocomposite to Eliminate Rhodamine-B Dye from Aqueous Medium. *Molecules* **2023**, *28*, 176. [CrossRef] [PubMed]
40. Tseng, S.-J.; Huang, Y.-S.; Wu, Q.-Y.; Wang, W.-L.; Wu, J.J. Hollow-structured Pd/TiO_2 as a dual functional photocatalyst for methyl orange oxidation and selective reduction of nitrate into nitrogen. *J. Ind. Eng. Chem.* **2023**, *119*, 386–394.
41. Zhang, S.; Lei, C.; Song, L. Chiral induction enhanced photocatalytic degradation of methyl orange by Ag@Ag_3PO_4 and the reaction mechanism. *Ceram. Int.* **2023**, *49*, 26548–26557. [CrossRef]
42. Bi, T.; Du, Z.; Chen, S.; He, H.; Shen, X.; Fu, Y. Preparation of flower-like ZnO photocatalyst with oxygen vacancy to enhance the photocatalytic degradation of methyl orange. *Appl. Surf. Sci.* **2023**, *614*, 156240. [CrossRef]
43. Khan, K.A.; Shah, A.; Nisar, J.; Haleem, A.; Shah, I. Photocatalytic Degradation of Food and Juices Dyes via Photocatalytic Nanomaterials Synthesized through Green Synthetic Route: A Systematic Review. *Molecules* **2023**, *28*, 4600. [CrossRef] [PubMed]
44. Haleem, A.; Shafiq, A.; Chen, S.Q.; Nazar, M. A Comprehensive Review on Adsorption, Photocatalytic and Chemical Degradation of Dyes and Nitro-Compounds over Different Kinds of Porous and Composite Materials. *Molecules* **2023**, *28*, 1081. [CrossRef] [PubMed]
45. Haleem, A.; Chen, S.Q.; Pan, J.M.; He, W.D. Gamma radiation induced synthesis of double network hydrophilic cryogels at low pH loaded with AuNPs for fast and efficient degradation of Congo red. *J. Hazard. Mater. Adv.* **2023**, *10*, 100299. [CrossRef]